Tunable Planar Focusing Based on Hyperbolic Phonon Polaritons in α-MoO_3

Yunpeng Qu, Na Chen, Hanchao Teng, Hai Hu, Jianzhe Sun, Renwen Yu, Debo Hu, Mengfei Xue, Chi Li, Bin Wu, Jianing Chen, Zhipei Sun, Mengkun Liu, Yunqi Liu, F. Javier García de Abajo, and Qing Dai**

Manipulation of the propagation and energy-transport characteristics of subwavelength infrared (IR) light fields is critical for the application of nanophotonic devices in photocatalysis, biosensing, and thermal management. In this context, metamaterials are useful composite materials, although traditional metal-based structures are constrained by their weak mid-IR response, while their associated capabilities for optical propagation and focusing are limited by the size of attainable artificial optical structures and the poor performance of the available active means of control. Herein, a tunable planar focusing device operating in the mid-IR region is reported by exploiting highly oriented in-plane hyperbolic phonon polaritons in α-MoO_3. Specifically, an unprecedented change of effective focal length of polariton waves from 0.7 to 7.4 μm is demonstrated by the following three different means of control: the dimension of the device, the employed light frequency, and engineering of phonon–plasmon hybridization. The high confinement characteristics of phonon polaritons in α-MoO_3 permit the focal length and focal spot size to be reduced to 1/15 and 1/33 of the incident wavelength, respectively. In particular, the anisotropic phonon polaritons supported in α-MoO_3 are combined with tunable surface-plasmon polaritons in graphene to realize in situ and dynamical control of the focusing performance, thus paving the way for phonon-polariton-based planar nanophotonic applications.

1. Introduction

Subwavelength optical focusing has been extensively exploited to concentrate electromagnetic energy down to nanoscale regions and achieve large field enhancement, thus opening promising application prospects in optical imaging,[1] biosensing,[2] photocatalysis,[3] nonlinear optics,[4] and manipulation of nanoscale energy flow.[5] In particular, in-plane subwavelength focusing is a critical element for realizing integrated nano-optics devices that enable applications in planar photonics,[6] such as nanoscale imaging, enhanced spectroscopy, and nanolithography. Metamaterials[6a–c,g–i] are the most commonly used composite materials to construct planar hyper-lenses and achieve in-plane subwavelength focusing. However, the focal distance and focal spot size are limited by the feature size in these artificial materials, and most nanostructures offer poor chances to modulate the focal spot, so that the achievement

Y. Qu, N. Chen, H. Teng, H. Hu, D. Hu, C. Li, Q. Dai
CAS Key Laboratory of Nanophotonic Materials and Devices
CAS Key Laboratory of Standardization and Measurement for Nanotechnology
CAS Center for Excellence in Nanoscience
National Center for Nanoscience and Technology
Beijing 100190, P. R. China
E-mail: huh@nanoctr.cn; daiq@nanoctr.cn

Y. Qu, Q. Dai
Sino-Danish College
University of Chinese Academy of Sciences
Beijing 100049, P. R. China

N. Chen, H. Teng, H. Hu, D. Hu, C. Li, Q. Dai
School of Nanoscience and Technology
University of Chinese Academy of Sciences
Beijing 100049, P. R. China

J. Sun, B. Wu, Y. Liu
Beijing National Laboratory for Molecular Sciences
Key Laboratory of Organic Solids
Institute of Chemistry
Beijing 100190, P. R. China

R. Yu,[+] F. J. García de Abajo
ICFO-Institut de Ciencies Fotoniques
The Barcelona Institute of Science and Technology
Castelldefels (Barcelona) 08860, Spain

M. Xue
Wenzhou Institute
University of Chinese Academy of Sciences
Wenzhou 325001, China

M. Xue, J. Chen
The Institute of Physics
Chinese Academy of Sciences
Beijing 100190, China

M. Xue
School of Physical Sciences
University of Chinese Academy of Sciences
Beijing 100049, P. R. China

of ultra-small resolution becomes difficult.[7] As a result, their active modulation remains as a challenging task that demands urgent attention. Moreover, the operation regime is limited to the ultraviolet (UV) to the near-infrared (IR) spectral range when relying on metals as constitutive materials, which present a weak mid-IR polarization response.[6c]

Polaritons are commonly described as quasiparticles of hybrid light-matter nature, enabling light trapping at the nanoscale, deep below the optical wavelength. The roadmap for polaritons has been dramatically enriched by the emergence of van der Waals (vdW) materials that are attracting substantial research attention because of their potential photonic and optoelectronic applications.[8] These vdW materials support various types of surface modes, including plasmon polaritons involving the collective motion of charge carriers in conductors,[5a,6d,9] atomic vibrations (phonons) in polar insulators,[10] excitons in semiconductors,[11] cooper pairs in superconductors,[12] and spin resonances in (anti-)ferromagnets.[13] Among them, phonon polaritons (PhPs) feature ultra-low inelastic losses, highly confined light fields, and strong stability at room temperature.[10] Also, confined electromagnetic waves coupled to phonons in hyperbolic dielectrics are referred to as hyperbolic phonon polaritons (HPhPs).[14] In particular, orthorhombic molybdenum trioxide (α-MoO_3)[10b] and vanadium pentoxide (α-V_2O_5)[10c] have been demonstrated to support biaxial HPhPs with extreme anisotropy in the mid-IR to terahertz spectral region (corresponding to energies ranging from molecular vibrations to thermal emission and absorption), which stems from their highly anisotropic lattice vibrations along different principal axes. In contrast to artificial surfaces, these natural hyperbolic two-dimensional (2D) materials support higher wave vectors and electromagnetic confinement in the hyperbolic regime and, thus, offer potential advantages in planar focusing.[10a,15] Moreover, vdW materials configure a platform that allows for the fabrication of heterostructures with a plethora of appealing properties via stacking of weakly bonded atomic layers, facilitating the design of focusing structures, and providing a rich range of possibilities for active control.[16]

Recently, several pioneering studies have revealed the potential of HPhPs of α-MoO_3 in the field of planar focusing,[17] and in-depth analyses of this phenomenon have been proposed.[17c,d] In this study, the highly integrated planar focusing of HPhP propagating on the surface of the α-MoO_3 flakes in the IR range is demonstrated. Using gold disks as nanoantennas to couple external light to HPhPs (which has been previously implemented in uniaxial hexagonal boron nitride (*h*-BN)),[18] a focal length as low as 700 nm and a focal spot size of 323 nm (≈1/33 of the incident wavelength) is simultaneously achieved. By changing the size of the gold disks and the frequency of incident light, the position of the focal point can be controlled over one order of magnitude, from 0.7 to 7.4 μm. Furthermore, a graphene/α-MoO_3 heterostructure is designed to demonstrate active control over HPhP focusing by changing the graphene Fermi energy. Our findings open new vistas for tunable planar focusing of mid-IR HPhPs based on planar antennas fabricated on α-MoO_3, with potential application in chemical sensing and thermal management.

Z. Sun
Department of Electronics and Nanoengineering
Aalto University
Espoo FI-02150, Finland

Z. Sun
QTF Centre of Excellence Department of Applied Physics
Aalto University
Aalto FI-00076, Finland

M. Liu
Department of Physics and Astronomy
Stony Brook University
Stony Brook, NY 11794, USA

F. J. García de Abajo
ICREA-Institució Catalana de Recerca i Estudis Avançats
Passeig Lluís Companys 23, Barcelona 08010, Spain

2. Results

2.1. Planar Focusing of Hyperbolic Polaritons in α-MoO_3

In conventional optics, according to the Huygens–Fresnel principle, wave propagation can be regarded as the interference and superposition of spherical waves emitted by each point on the wavefront as a wavelet source. Further, considering the time-reversal symmetry of the wave, the wavefront of a point excitation serves as a new wavelet source that generates a wave converging at the original excitation point. Similarly, the use of concave antennas or convex lenses can aid in achieving planar focusing in in-plane isotropic polaritons, such as plasmons in graphene[6d] and PhPs in *h*-BN.[6k]

α-MoO_3 is a natural hyperbolic material with a highly anisotropic response in the mid-IR to terahertz spectral region, featuring three mid-IR Reststrahlen bands (the frequency region between transverse and longitudinal optical phonons), where PhPs can exist:[10,19a,b] band I at ω = 542–856 cm^{-1} for [001] phonons ($\varepsilon_x > 0$, $\varepsilon_y < 0$ and $\varepsilon_z > 0$); band II at ω = 816–976 cm^{-1} for [100] phonons ($\varepsilon_x < 0$, $\varepsilon_y > 0$ and $\varepsilon_z > 0$); and band III at ω = 956–1012 cm^{-1} for [010] phonons ($\varepsilon_x > 0$, $\varepsilon_y > 0$ and $\varepsilon_z < 0$) (Figure S1a, Supporting Information). As a result, PhPs in natural α-MoO_3 exhibit both elliptic and hyperbolic in-plane dispersion. The different modes can be described by an isofrequency curve (IFC) at a specific incident frequency (more details are presented in Note 1, Supporting Information). **Figure 1**a shows that, for PhPs in an α-MoO_3 film at the mid-IR frequency ω_0 = 910 cm^{-1}, hyperbolic PhPs can propagate only if $|\tan\varphi| \leq \sqrt{-\varepsilon_y / \varepsilon_x}$. Therefore, focusing of HPhPs in α-MoO_3 can be realized with convex antennas, in contrast to focusing of isotropic electromagnetic waves that follow the Huygens–Fresnel principle.

To validate this prediction, a gold disk is used herein to excite and focus the HPhPs of α-MoO_3 (Figure 1b). The simulation substantiates that the PhPs launched by a gold disk converge on a focal point (Figure 1c). Through coupling to IR light, each point along the edge of the gold disk can be regarded as a wavelet source, and waves from all such wavelets interfere with each other. Based on this construction, the focus is located at the intersection of Poynting vectors $\vec{S}$ tangent to the gold disk (green arrow in Figure 1c, corresponding to a high wave vector $\vec{k}$ (red arrow in Figure 1a) and perpendicular to the asymptote of the IFC, i.e., $\theta = \frac{\pi}{2} - \varphi$). Based on this simple geometrical analysis, the focal length f can be expressed as follows:

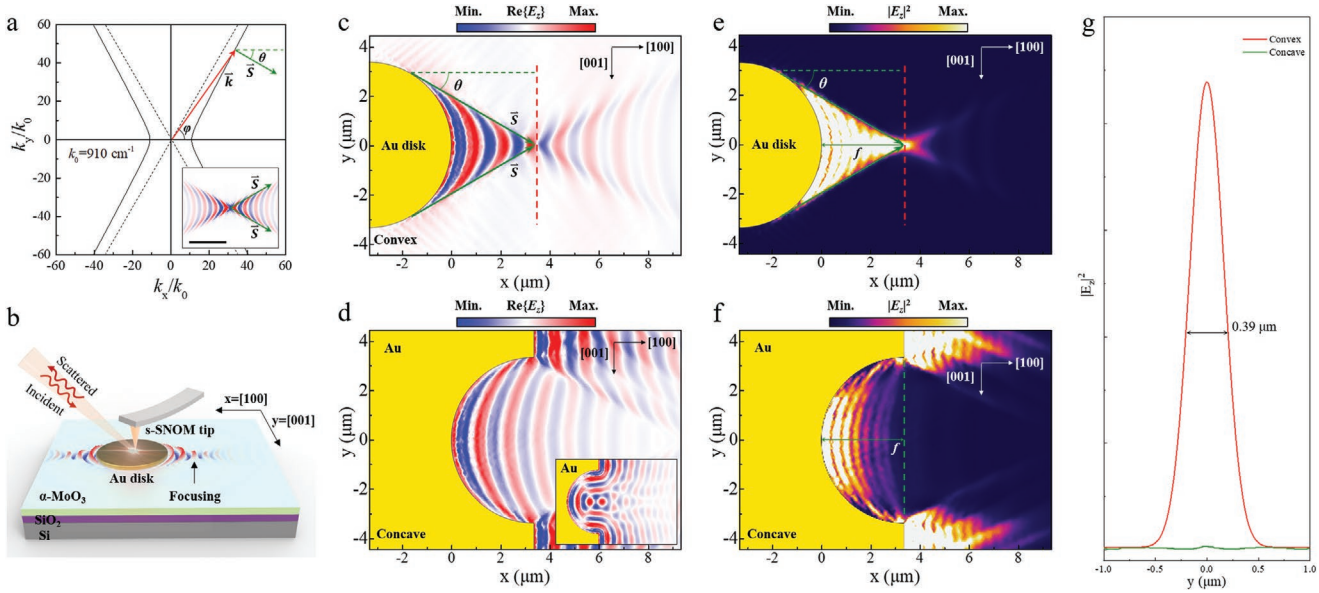

Figure 1. Conceptual design of planar focusing of HPhPs in α-MoO_3. a) IFC of HPhPs in a 262-nm-thick α-MoO_3 crystal under excitation by light of frequency ω_0 = 910 cm^{-1}. The Poynting vector $\vec{S}$ associated with PhPs at high wave vector $\vec{k}$ is nearly perpendicular to the asymptote of the IFC. The inset shows the real-space propagation of PhPs launched by a dipole, where the Poynting vectors $\vec{S}$ (green arrows) are shown to be consistent with that in the IFC. b) Experimental scheme for launching and planar focusing of HPhPs in an α-MoO_3 film by s-SNOM. c) Simulated real part of the near-field distribution Re{E_z} of HPhPs in α-MoO_3, launched by a gold disk at a frequency of 910 cm^{-1}. The intersection of Poynting vectors $\vec{S}$ (green arrows) indicates the focus of the antenna. d) Similar to (c) but using a concave gold antenna with the same radius as the gold disk shown in (c), which shows no evidence of focusing. The inset shows focusing of PhPs by a concave gold antenna in a film with in-plane isotropic permittivity $\varepsilon_x = \varepsilon_y = -3.0 + 0.16i$. e) Simulated distribution of electric field intensity $|E_z|^2$ derived from (c). f) Simulated distribution of $|E_z|^2$ derived from (d). g) Electric field intensity along with the corresponding red (green) dashed lines in (e) and (f).

$$f = \frac{R}{\sin\theta} - R = R\sqrt{1+\frac{1}{\tan^2\theta}} - R = R\left(\sqrt{1-\frac{\varepsilon_x}{\varepsilon_y}} - 1\right) \quad (1)$$

where R is the radius of the gold disk and the focal length herein is defined as the shortest distance from the edge of the gold disk. Note that, although the thickness of α-MoO_3 affects the propagation of PhPs (Figure S2g, Supporting Information), such influence can be ignored when the α-MoO_3 film is sufficiently thin (less than 300 nm).

To verify that only a convex antenna can produce a focusing effect in planar anisotropic α-MoO_3, PhPs launched by a concave gold antenna are simulated in this study. Figure 1d illustrates that there is no evidence of focusing of PhPs launched by the concave antenna in the anisotropic plane compared with the isotropic plane. Comparative analysis of the energy distribution of the electric field generated by the excitation of the convex and concave antennas (shown in Figure 1e) further confirms that the concave one does not exhibit a focusing effect on the PhPs in α-MoO_3.

Propagation angles of the HPhPs have a limited range; therefore, most of the electromagnetic energy is increasingly confined between the focal point and the gold disk, thereby leading to a high electric field enhancement compared with focusing by an isotropic plane. Owing to the contribution of spherical aberration (SA) and the diffraction limit of surface waves, the real focus is a spot of finite size instead of just a point, and this size can be considered as the superposition of the transverse spherical aberration (TSA) and the optical resolution limit of surface waves. The full width at half maximum (FWHM) is obtained at the focal spot by Gaussian fitting of the electric field intensity along the y axis (Figure 1f), which renders a value of 0.39 μm, corresponding to 1/28 of the excitation light wavelength (λ_0 = 10.99 μm) and, thus, revealing a deep subwavelength compression.

2.2. Controlling the Focusing Performance of HPhPs by Varying the Gold-Disk Diameter

Equation (1) indicates that the focal distance f of HPhPs in α-MoO_3 should be proportional to the radius R of the employed gold disk. To experimentally corroborate the regulating effect of the gold disk size on the focal distance of in-plane HPhPs, a series of different structures with different sizes of gold-disk antennas (diameters from 0.5 to 22 μm) was fabricated to excite the polaritons (**Figure 2**a). A scattering-type scanning near-field optical microscope (s-SNOM) was used to image the propagation and focusing of HPhPs in α-MoO_3 with different sizes of the gold-disk antennas.

The images obtained for three different diameters (D = 15, 11, and 6.7 μm) of gold-disk antennas at a fixed frequency (ω_0 = 910 cm^{-1}) are shown in Figure 2b. Importantly, all the experimental results corroborate that the HPhPs launched by the gold-disk antennas propagate along the [100] α-MoO_3 direction and are increasingly focused with propagation distance, eventually leading to the formation of a focal spot. Moreover, the near-field images are in excellent agreement with full-wave numerical simulations, as shown in Figure 2c

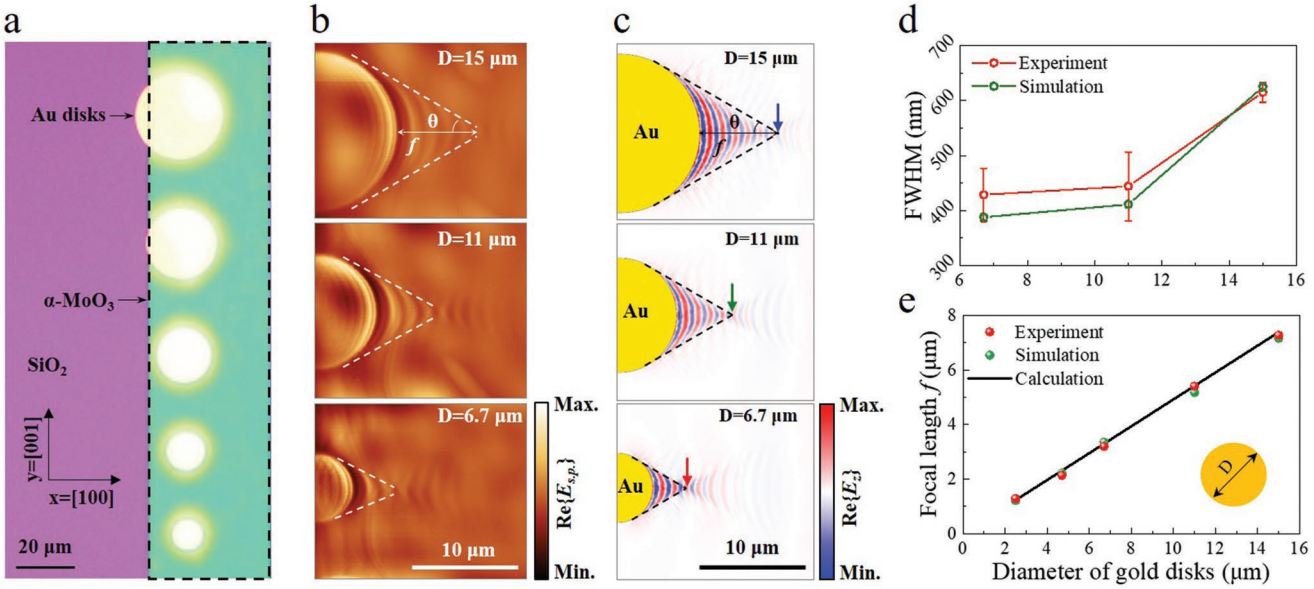

Figure 2. Controlling the focusing performance of HPhPs in α-MoO_3 by varying the gold disk diameter. a) Optical microscopy images of gold disks of different diameters under the α-MoO_3 flake. The α-MoO_3 flake is marked by the dashed lines. b) Measured near-field optical images of the focusing of HPhPs with varying diameters of gold disks. The frequency of the incident light is $\omega_0 = 910$ cm^{-1}. The intersections of dashed lines indicate the focus of the antennas. c) Simulated real part of the near-field distribution Re$\{E_z\}$ at a frequency of 910 cm^{-1} launched by gold disks corresponding to (b). d) FWHM of the focal spots for different gold disk diameters extracted from experiments (b) and simulations (c). e) Dependence of the experimental, simulated, and analytically calculated values of the focal length f versus gold-disk diameter D.

and Figure S3, Supporting Information. The TSA is directly proportional to the size of the antennas;[20] therefore, the FWHM of the focus size increases with increasing diameter of the gold disks, from 0.39 μm for D = 6.7 μm to 0.62 μm for D = 15 μm, as shown in Figure 2d and Figure S4a, Supporting Information. Noteworthy, the electric field intensity at the focus decreases significantly with increasing disk size (Figure S4a, Supporting Information). As a result, the coupling efficiency of gold disks with different diameters (see details in Note 2, Supporting Information) can be further estimated. Figure S5, Supporting Information demonstrates that when the diameter of the disk is greater than 3 μm, its coupling efficiency decreases with increasing size, and gradually approaches a certain value. The focal distances f obtained from the experimental and simulation results are indicated by red and green dots in Figure 2e, respectively. The solid black line shows the focal distance obtained from the analytical calculation performed by using Equation (1). Both the experimental and numerical simulation results show a linear dependence that is consistent with the analytical prediction of Equation (1).

In addition to gold-disk antennas, circular holes on the silica (SiO_2) substrate could also achieve similar focusing performance, in which HPhPs are launched by the edge of the hole, and the focal length f follow the same linear dependence on the hole diameter as with the gold disks (Figures S6 and S7, Supporting Information). However, when using holes, the excitation structure no longer occupies extra space in the vertical direction caused by the thickness of gold disks (Figure S7c,d, Supporting Information), thus realizing the focusing effect in the same absolute plane (Figure S7e,f, Supporting Information).

2.3. Controlling the Focusing Performance of HPhPs in α-MoO_3 by Varying the Light Frequency

Careful examination of the dielectric function of α-MoO_3 indicates that the permittivity of each principal axis changes direction with the frequency of the incident light, as shown in Figure S1a, Supporting Information. First, the in-plane permittivity ε_x and ε_y aids in the determination of the angular range of HPhPs propagation (i.e., $|\tan\varphi| \leq \sqrt{-\varepsilon_y/\varepsilon_x}$), which in turn affects the focusing distance. Second, the IFC shifts along the x axis with varying frequency, thus leading to a change in the polaritonic wavelength and, consequently, the focus size.

In this study, incident light with different frequencies between 892 and 950 cm^{-1} is used to illuminate the sample with a gold disk diameter of 6.7 μm (Figure 2a). The images obtained under three different incident frequencies (ω_0 = 892, 910, and 930 cm^{-1}) are shown in **Figure 3**a. With the increase in frequency, the focusing point gradually approaches the gold disk, and the focal positions become consistent with our full-wave numerical simulation results, as shown in Figure 3b. As mentioned above, the propagation boundaries of HPhPs (i.e., the tangents to the gold disk through the focal point) correspond to the Poynting vector $\vec{S}$ at high wave vector $\vec{k}$ under a given wavenumber k_0. Figure 3c shows the IFC diagram with wavenumbers corresponding to Figure 3a, where the labeled Poynting vectors $\vec{S}$ have the same slopes with HPhPs propagation boundaries as obtained from experiment (white dashed lines in Figure 3a) and simulation (black dashed lines in Figure 3b) at the corresponding frequencies.

The FWHM of the focus size decreases from 0.46 μm at ω_0 = 892 cm^{-1} to 0.32 μm at ω_0 = 930 cm^{-1}, as shown in Figure 3d, which is positively correlated with the polariton

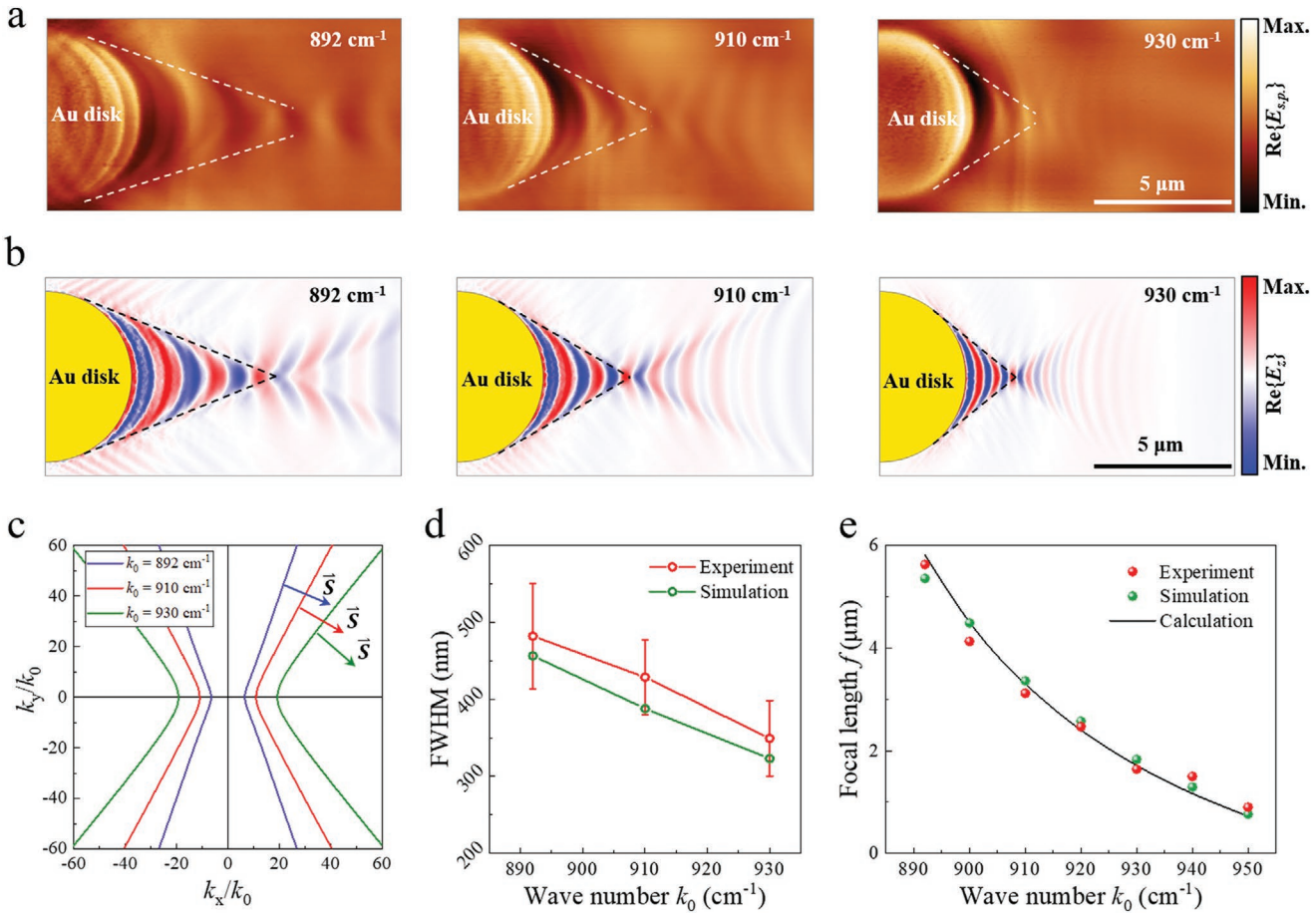

Figure 3. Controlling the focusing performance of HPhPs in α-MoO_3 by varying the light frequency. a) Measured near-field optical images of the focusing of HPhPs with different incident light frequencies. The diameter of the gold disk is 6.7 μm. b) Simulated real part of the near-field distribution Re$\{E_z\}$ at frequencies corresponding to (a). c) IFC of HPhPs in a 262 nm-thick α-MoO_3 crystal under excitation light of frequencies corresponding to (a). d) FWHM of the focal spot at different frequencies extracted from (a) and (b). The simulated focus sizes are extracted from $|E_z|^2$ as shown in Figure S4b, Supporting Information. e) Dependence of the experimental, simulated, and analytically calculated values of the focal length f versus the wavenumber k_0 of the incident light.

wavelength λ_p, according to the optical resolution limit $d = \lambda_p/2NA$. Figure 3e shows the relationship between the focal length f and the wavenumber k_0 of the incident light. When the incident frequency is tuned from 892 to 950 cm^{-1}, the focal length f shifts from about 0.95 to 5.8 μm. Notably, the focal length maintains a good degree of linearity with the diameter of the gold disks under different incident light frequencies (Figure S8, Supporting Information). However, when the incident frequency exceeds 950 cm^{-1}, close to the Reststrahlen band III, the in-plane PhPs tend to evolve toward elliptical modes, and the focusing performance undergoes rapid degradation.

2.4. Active Control over the Focusing Performance of SPP-PhPs in Graphene/α-MoO_3 Heterostructures by Changing the Graphene Fermi Energy

Graphene is a well-studied vdW material that can effectively support surface-plasmon polaritons (SPPs) formed by the hybridization of photons and electrons, with a broad response frequency range and susceptibility to electrical tunability. Noteworthy, these unique optical response characteristics are derived from the peculiar conical band structure of graphene with zero bandgap, that is, the momentum and energy of its electrons are linearly related. Therefore, the properties of SPPs can be tuned dynamically by changing the Fermi energy of graphene, which can be achieved by applying a gate voltage[21] and also via chemical doping.[22a,b] In order to further exploit this property of graphene, multiple studies have realized the excitation and modulation of in-plane isotropic SPP-PhPs in graphene/h-BN heterostructures.[16b,c] Compared with h-BN, α-MoO_3 can support in-plane hyperbolic PhPs, and the hybridization with the isotropic SPPs of graphene leads to effective modulation of the focusing performance, as explored previously.[22b]

Herein, following a previous study,[22b] a hybrid plasmon–phonon polariton between graphene and α-MoO_3 vdW heterostructures interface is designed to reconfigure and engineer the in-plane hyperbolic response (as shown in Figures 4a,b). The hybrid mode is driven by electromagnetic hybridization between isotropic SPPs in the top graphene monolayer and directional PhPs in the bottom α-MoO_3 film.[22] According to our theoretical calculations (details presented in Note 3 and

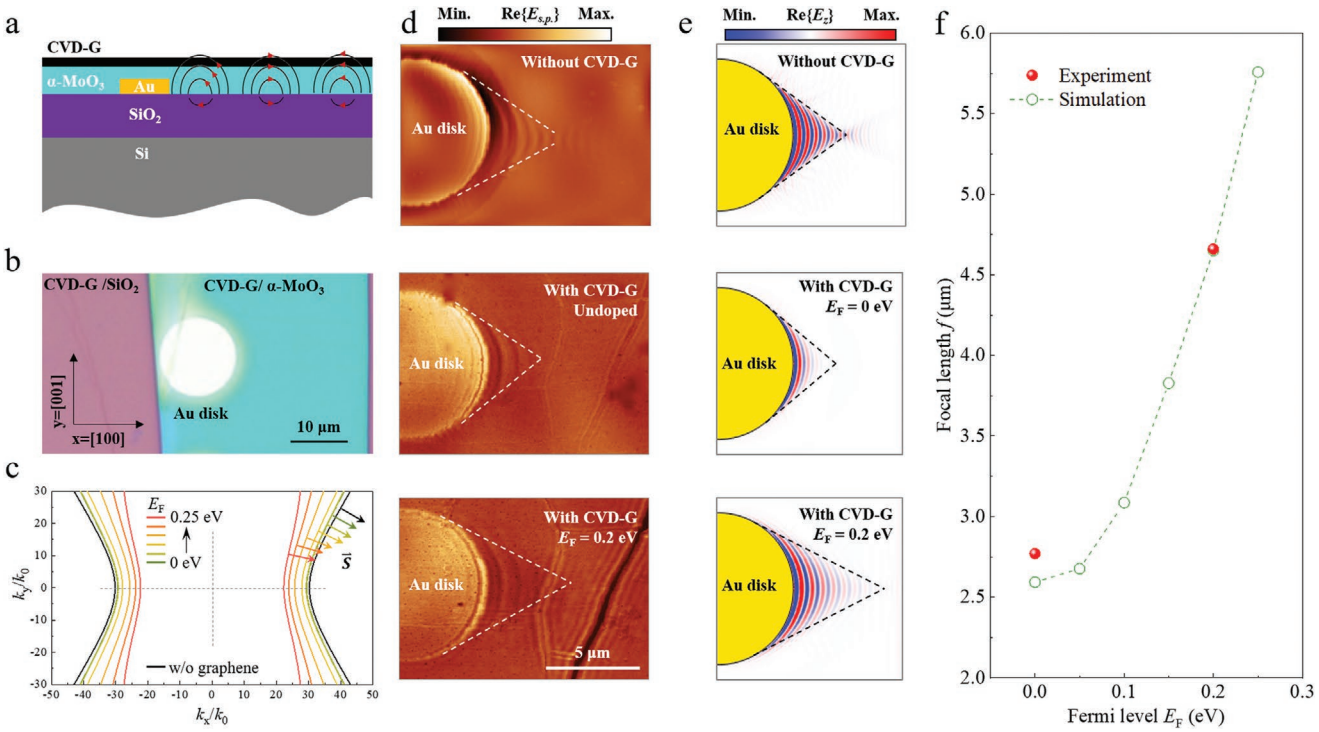

Figure 4. Active control over the focusing performance of SPP-PhPs in graphene/α-MoO_3 heterostructures by changing the graphene Fermi energy. a) Schematic representation of a graphene/α-MoO_3 heterostructure and excitation of SPP-PhPs. b) Optical microscopy images of CVD-graphene-covered α-MoO_3 decorated with a gold disk. The thickness of α-MoO_3 is 123 nm. c) IFC of SPP-PhPs under excitation with light of frequency ω_0 = 920 cm^{-1} in a graphene/α-MoO_3 heterostructure at different Fermi energies of graphene. d) Near-field optical images of the focusing of HPhPs in α-MoO_3 without CVD-graphene and focusing of SPP-PhPs in graphene/α-MoO_3 at different Fermi energies of graphene. The frequency of the incident light is 920 cm^{-1}. e) Simulated real part of Re{E_z}, corresponding to (d). f) Dependence of the experimental and simulated values of the focal length f versus the graphene Fermi energy E_F.

Figure S9, Supporting Information), when increasing the graphene Fermi energy, the IFC of the SPP-PhPs shifts toward the lower wave vector direction along the x axis (**Figure 4**c). At the same time, the shape of the IFC gradually expands along the y axis thus narrowing the range of propagation angles φ (Figure 4c). In particular, at high wave vector angle φ, the IFC changes from outward bending to inward bending (taking the origin point as a reference), and exhibits a minimum slope and zero curvature at the transition point. For convex antennas, only wave vectors with outward IFC curvature contribute to focusing (analogous to the behavior of pure α-MoO_3), while the part with inward curvature causes the wavefront to diverge (as in the case of isotropic media).[18] Therefore, unlike HPhPs in α-MoO_3, the propagation boundaries of SPP-PhPs in the graphene/α-MoO_3 heterostructure no longer correspond to the Poynting vector $\vec{S}$ at high wave vector $\vec{k}$, but to the Poynting vector $\vec{S}$ with the largest angle θ relative to the x axis, as shown in Figure 4c. According to the 2D fast Fourier transform (2D-FFT) of the simulated near-field distribution (shown in Figure S10b, Supporting Information), the intensity of wave vectors launched by the gold disk is mainly concentrated along small angles below the transition point, indicating that the energy of wave vectors at higher angles is divergent.

The Fermi energy of graphene is effectively tuned by doping with NO_2 gas[23] (see Experimental Section), and quantified by Raman spectroscopy (Figure S11, Supporting Information). Figure 4d and Figure S12, Supporting Information show near-field images of the same α-MoO_3 sample with and without chemical vapor deposition (CVD) graphene under 920 cm^{-1} light irradiation. The focal length f of the observed HPhPs in α-MoO_3 is 2.80 μm, and then f is slightly decreased to 2.77 μm after covering with undoped graphene, while it further increases to 4.66 μm when the graphene is doped to a Fermi energy E_F = 0.2 eV. The simulation results (Figure 4e and Figure S10a, Supporting Information) indicate that the focal length f of SPP-PhPs increases exponentially with increasing graphene Fermi energy E_F (Figure 4f). It is worth noting that, owing to the finite doping of the wet-transferred CVD graphene, the experimental focal length (2.77 μm) is slightly greater than the simulated one (2.59 μm) at a Fermi energy of 0 eV. The simulation results (Figure S13, Supporting Information) further indicate that the focus size decreases slightly with increasing Fermi energy, mainly because of the high dissipation of polaritons at low Fermi energy. In contrast, when the Fermi energy is higher, the focus size increases, which may be due to the influence of divergent polaritons.

3. Conclusions

A new type of planar focusing device in the mid-IR range was demonstrated using highly oriented in-plane HPhPs in α-MoO_3, launched by a metal antenna with tailored geometries.

By changing the antenna structure, incident light frequency, and α-MoO_3 thickness, the focal length and focus size could cover a wide range extending from 700 nm to 7.4 μm. In particular, the anisotropic PhPs supported in α-MoO_3 were combined with tunable SPPs in graphene to further realize in situ and dynamical focusing control performance. Furthermore, the characteristic high confinement of PhPs in α-MoO_3 resulted in a decrease in the focal length and focal spot size down to just 1/15 and 1/33 of the incident wavelength, respectively.

This highly compressed focusing effect could effectively increase the interaction between IR light and matter, which could be advantageous in planar photonics and further benefit the design of integrated nano-optical systems, such as on-chip selective waveguides, optical routing, and beam splitting into subwavelength scales. Notably, the mid-IR region encompasses molecular vibrational energies and thermal radiation; therefore, this focusing effect, causing near-field enhancement and high energy density, can increase light–matter interaction, making it more versatile for photocatalysis, biological detection, spontaneous emission, and thermal energy management. Finally, the focusing tunability of phonon polaritons in α-MoO_3 also provides a promising platform for exploring other types of anisotropic polaritons in vdW materials.

4. Experimental Section

Theoretical Modeling and Numerical Simulations: In this study, full-wave simulations were carried out by the finite-element method in COMSOL Multiphysics. The structures were modeled as an α-MoO_3 film of specific thickness on the top of a 500 nm-thick SiO_2 substrate with a 1000 nm-thick air layer above it. A 60-nm-thick gold disk was placed between the α-MoO_3 film and the SiO_2 substrate, replacing the corresponding part of the α-MoO_3 to minimize its deformation. During the simulation, the model without the gold disk was first illuminated with a plane wave normally impinging on the surface with linear polarization along the [100] axis of α-MoO_3. Subsequently, the obtained electric field was applied as a background field to the model with the gold disk. The real part of the vertical component of the electric field $\mathrm{Re}\{E_z\}$ was collected from 10 nm above the α-MoO_3 surface to obtain the near-field images. The focusing of HPhPs launched by holes in the SiO_2 substrate was simulated by following the same method but replacing the gold disk in α-MoO_3 with an air hole in SiO_2. The permittivity of α-MoO_3 was described by using the Lorentz model[19] (details are presented in Note 4 and Table S2, Supporting Information), while the dielectric constants of SiO_2[24] and gold[25] were obtained from the database in COMSOL (Figure S1c,d, Supporting Information).

To simulate the graphene/α-MoO_3 heterostructure, graphene was modeled as a homogenous 2D conducting layer with complex conductivity ($\sigma = \sigma_{\mathrm{intra}} + \sigma_{\mathrm{inter}}$) given by the Kubo formula[26] as follows:

$$\sigma = \frac{ie^2 E_F}{\pi\hbar^2\left(\omega + i\tau^{-1}\right)} + \frac{ie^2}{4\pi\hbar}\ln\left[\frac{2|E_F| - \hbar\left(\omega + i\tau^{-1}\right)}{2|E_F| + \hbar\left(\omega + i\tau^{-1}\right)}\right] \tag{2}$$

where $\omega = 2\pi\nu$ is the angular frequency and $\tau = \mu E_F/e{v_F}^2$ denotes the relaxation time. The Fermi velocity v_F was set to $c/300 = 10^6$ m s^{-1}, and the carrier mobility μ of graphene was assumed to be 2000 cm^2 V^{-1} s^{-1}. The graphene permittivity was defined as follows:

$$\varepsilon_g = 1 + \frac{i\sigma}{\omega\varepsilon_0 t_g} \tag{3}$$

where t_g represents the thickness of graphene, which was set to 1 nm-thick in the simulations of graphene placed at the interface between α-MoO_3 and air. Furthermore, the Fermi energy E_F of graphene was varied to regulate the focusing performance.

Sample Fabrication: The gold-antenna arrays (diameters ranging from 0.5 to 22 μm) were fabricated by electron-beam evaporation of 5 nm of titanium and 60 nm of gold in vacuum ($<5 \times 10^{-6}$ Torr) onto a commercial silicon (Si) wafer (SVM, Inc., with a 300 nm SiO_2 layer) with ≈350 nm of PMMA950K resist that was pre-patterned by electron-beam lithography (EBL, 100 kV, Vistec 5000+ES, Germany). The electron-beam resist was removed by using a hot acetone bath at 70 °C for 25 min and a gentle rinse with isopropyl alcohol (IPA) for 3 min, followed by nitrogen gas drying and thermal baking.

Circular holes (Figure S6a, Supporting Information) were patterned on the 300-nm SiO_2/500 μm Si wafer (SVM, Inc.) by EBL on approximately 350-nm ZEP520A resist and etched with C_4F_8 and SF_6 gases (North Microelectronics, DSE200). The resist layer was dissolved with butanone, and the entire wafer was then cleaned with IPA.

High-quality α-MoO_3 flakes were mechanically exfoliated from bulk crystals prepared by CVD by following the previously reported methods,[27] and the selected flakes were transferred onto gold antenna arrays (Figure 2a and Figures S7a and S8a, Supporting Information) or circular holes (Figures S6b and S7b, Supporting Information), respectively. The lattice direction of α-MoO_3 was determined through optical microscopy, because α-MoO_3 crystals grow naturally into anisotropic rectangular flakes with dimensions [001] >> [100] >> [010].[10b]

Monolayer graphene was grown on Cu foil by CVD and transferred onto α-MoO_3 samples through a poly(methyl methacrylate) (PMMA) assisted method[28] (Figure 4b). The Fermi energy of graphene was tuned by placing samples in a chamber with NO_2 gas molecules for several hours.

s-SNOM Measurements: The near field was measured using a scattering SNOM setup (Neaspec GmbH) equipped with wavelength-tunable lasers (between 890 and 2000 cm^{-1}). The incident p-polarized IR light from a tunable CO_2 laser was directed to a metalized tip (NanoWorld) of an atomic force microscope with an apex radius of ≈25 nm. The spot sizes of the mid-IR beam under the tip were made ≈20 μm in lateral size to cover the large area spanned by the antenna and the α-MoO_3 samples. The tip-tapping frequency and amplitudes were ≈270 kHz and ≈30–50 nm, respectively. Furthermore, the near-field amplitude images were obtained from the third-order demodulated harmonic of the scattering amplitude, which resulted in massive suppression of background noise. The focal position extracted from experiments is mainly based on the width of the electric field along the *y* axis, the hyperbolic boundary, and the electric field distribution along the *x* axis.

Acknowledgements

The authors acknowledge Dr. Pablo Alonso-González, Dr. Javier Martín-Sánchez, and Dr. Jiahua Duan (Departamento de Física, Universidad de Oviedo) for valuable discussions and constructive comments, and acknowledge Nanofab Lab @ NCNST for helping with sample fabrication. This work was supported by the National Key Research and Development Program of China (Grant No. 2020YFB2205701), the National Natural Science Foundation of China (Grant Nos. 51902065, 52172139, 51925203, U2032206, 52072083, and 51972072), Beijing Municipal Natural Science Foundation (Grant No. 2202062), and Strategic Priority Research Program of Chinese Academy of Sciences (Grant Nos. XDB36000000 and XDB30000000). F.J.G.A. acknowledges the ERC (Advanced Grant 789104-eNANO), the Spanish MICINN

(PID2020-112625GB-I00 and SEV2015-0522), and the CAS President's International Fellowship Initiative (PIFI) for 2021. Z.P.S. acknowledges the Academy of Finland (Grant Nos. 314810, 333982, 336144 and 336818), The Business Finland (ALDEL), the Academy of Finland Flagship Programme (320167,PREIN), the European Union's Horizon 2020 research and innovation program (820423,S2QUIP; 965124, FEMTOCHIP), the EU H2020-MSCA-RISE-872049 (IPN-Bio), and the ERC (834742).

Conflict of Interest

The authors declare no conflict of interest.

Author Contributions

Y.Q., N.C., and H.T. contributed equally to this work. Q.D. and H.H. conceived the idea. Q.D. and H.H. led the experiments. Y.Q., H.T., and R.Y. developed the theory. Y.Q. and H.T. performed the simulation. H.H. and N.C. designed the structures and prepared the samples. H.H. and N.C. performed the near-field measurements. H.H., H.T., Y.Q., and N.C. analyzed the data. All authors discussed the results. Finally, Y.Q. and H.H. wrote the manuscript, with input and comments from all authors.

Keywords

α-MoO_3, hyperbolic materials, phonon polaritons, planar subwavelength focusing, tunable focusing

[1] a) X. U. Ting, A. Agrawal, M. Abashin, K. J. Chau, H. J. Lezec, *Nature* **2013**, *497*, 470; b) M. Khorasaninejad, W. T. Chen, R. C. Devlin, J. Oh, A. Y. Zhu, F. Capasso, *Science* **2016**, *352*, 1190.

[2] N. Liu, M. L. Tang, M. Hentschel, H. Giessen, A. P. Alivisatos, *Nat. Mater.* **2011**, *10*, 631.

[3] Y. Wang, L. Fang, M. Gong, Z. Deng, *Chem. Sci.* **2019**, *10*, 5929.

[4] a) S. Berweger, J. Atkin, X. Xu, R. Olmon, M. Raschke, *Nano Lett.* **2011**, *11*, 4309; b) S. Berweger, J. Atkin, R. Olmon, M. Raschke, *J. Phys. Chem. Lett.* **2012**, *3*, 945; c) M. Nielsen, X. Shi, P. Dichtl, S. Maier, R. Oulton, *Science* **2017**, *358*, 1179.

[5] a) X. Luo, T. Ishihara, *Appl. Phys. Lett.* **2004**, *84*, 4780; b) M. Schnell, P. Alonso-González, L. Arzubiaga, F. Casanova, L. E. Hueso, A. Chuvilin, R. Hillenbrand, *Nat. Photonics* **2011**, *5*, 283; c) D. K. Gramotnev, S. I. Bozhevolnyi, *Nat. Photonics* **2013**, *8*, 13.

[6] a) L. Verslegers, P. B. Catrysse, Z. Yu, S. Fan, *Phys. Rev. Lett.* **2009**, *103*, 033902; b) C. Ma, Z. Liu, *Opt. Exp.* **2010**, *18*, 4838; c) D. Lu, Z. Liu, *Nat. Commun.* **2012**, *3*, 1205; d) P. Alonso-González, A. Y. Nikitin, F. Golmar, A. Centeno, A. Pesquera, S. Vélez, J. Chen, G. Navickaite, F. Koppens, A. Zurutuza, F. Casanova, L. E. Hueso, R. Hillenbrand, *Science* **2014**, *344*, 1369; e) L. Yu, E. Barakat, T. Sfez, L. Hvozdara, J. Di Francesco, H. P. Herzig, *Light Sci. Appl.* **2014**, *3*, e124; f) A. Angelini, E. Barakat, P. Munzert, L. Boarino, N. De Leo, E. Enrico, F. Giorgis, H. P. Herzig, C. F. Pirri, E. Descrovi, *Sci. Rep.* **2014**, *4*, 5428; g) M. Kim, S. So, K. Yao, Y. Liu, J. Rho, *Sci. Rep.* **2016**, *6*, 38645; h) X. Wang, H. Chen, H. Liu, L. Xu, C. Sheng, S. Zhu, *Phys. Rev. Lett.* **2017**, *119*, 033902; i) L. Shen, L. J. Prokopeva, H. Chen, A. V. Kildishev, *Nanophotonics* **2017**, *7*, 479; j) M.-S. Kim, B. Vosoughi Lahijani, N. Descharmes, J. Straubel, F. Negredo, C. Rockstuhl, M. Häyrinen, M. Kuittinen, M. Roussey, H. P. Herzig, *ACS Photonics* **2017**, *4*, 1477; k) K. Chaudhary, M. Tamagnone, X. Yin, C. M. Spägele, S. L. Oscurato, J. Li, C. Persch, R. Li, N. A. Rubin, L. A. Jauregui, K. Watanabe, T. Taniguchi, P. Kim, M. Wuttig, J. H. Edgar, A. Ambrosio, F. Capasso, *Nat. Commun.* **2019**, *10*, 4487.

[7] K.-H. Chang, Y.-C. Chen, W.-H. Chang, P.-T. Lee, *Sci. Rep.* **2018**, *8*, 13648.

[8] P. Pons-Valencia, F. J. Alfaro-Mozaz, M. M. Wiecha, V. Biolek, I. Dolado, S. Vélez, P. Li, P. Alonso-González, F. Casanova, L. E. Hueso, L. Martín-Moreno, R. Hillenbrand, A. Y. Nikitin, *Nat. Commun.* **2019**, *10*, 3242.

[9] a) J. C. Weeber, J. R. Krenn, A. Dereux, B. Lamprecht, Y. Lacroute, J. P. Goudonnet, *Phys. Rev. B, Cond. Matter* **2001**, *64*, 045411; b) R. Won, *Nat. Photonics* **2009**, *3*, 500; c) T. J. Echtermeyer, S. Milana, U. Sassi, A. Eiden, M. Wu, E. Lidorikis, A. C. Ferrari, *Nano Lett.* **2016**, *16*, 8.

[10] a) S. Dai, Z. Fei, Q. Ma, A. S. Rodin, M. Wagner, A. S. McLeod, M. K. Liu, W. Gannett, W. Regan, K. Watanabe, T. Taniguchi, M. Thiemens, G. Dominguez, A. H. Castro Neto, A. Zettl, F. Keilmann, P. Jarillo-Herrero, M. M. Fogler, D. N. Basov, *Science* **2014**, *343*, 1125; b) W. Ma, P. Alonso-González, S. Li, A. Y. Nikitin, J. Yuan, J. Martín-Sánchez, J. Taboada-Gutiérrez, I. Amenabar, P. Li, S. Vélez, C. Tollan, Z. Dai, Y. Zhang, S. Sriram, K. Kalantar-Zadeh, S.-T. Lee, R. Hillenbrand, Q. Bao, *Nature* **2018**, *562*, 557; c) J. Taboada-Gutiérrez, G. Álvarez-Pérez, J. Duan, W. Ma, K. Crowley, I. Prieto, A. Bylinkin, M. Autore, H. Volkova, K. Kimura, T. Kimura, M. H. Berger, S. Li, Q. Bao, X. P. A. Gao, I. Errea, A. Y. Nikitin, R. Hillenbrand, J. Martín-Sánchez, P. Alonso-González, *Nat. Mater.* **2020**, *19*, 964.

[11] a) D. Fröhlich, E. Mohler, P. Wiesner, *Phys. Rev. Lett.* **1971**, *26*, 554; b) F. Hu, Y. Luan, M. E. Scott, J. Yan, D. G. Mandrus, X. Xu, Z. Fei, *Nat. Photonics* **2017**, *11*, 356; c) S. Klembt, T. H. Harder, O. A. Egorov, K. Winkler, R. Ge, M. A. Bandres, M. Emmerling, L. Worschech, T. C. H. Liew, M. Segev, C. Schneider, S. Höfling, *Nature* **2018**, *562*, 552.

[12] a) M. E. Berkowitz, B. S. Y. Kim, G. Ni, A. S. McLeod, C. F. B. Lo, Z. Sun, G. Gu, K. Watanabe, T. Taniguchi, A. J. Millis, J. C. Hone, M. M. Fogler, R. D. Averitt, D. N. Basov, *Nano Lett.* **2020**, *21*, 308; b) A. Dodel, A. Pikovski, I. Ermakov, M. Narozniak, V. Ivannikov, H. Wu, T. Byrnes, *Phys. Rev. Res.* **2020**, *2*, 013184.

[13] K. Grishunin, T. Huisman, G. Li, E. Mishina, T. Rasing, A. V. Kimel, K. Zhang, Z. Jin, S. Cao, W. Ren, G.-H. Ma, R. V. Mikhaylovskiy, *ACS Photon.* **2018**, *5*, 1375.

[14] G. Ni, A. S. McLeod, Z. Sun, J. R. Matson, C. F. B. Lo, D. A. Rhodes, F. L. Ruta, S. L. Moore, R. A. Vitalone, R. Cusco, L. Artús, L. Xiong, C. R. Dean, J. C. Hone, A. J. Millis, M. M. Fogler, J. H. Edgar, J. D. Caldwell, D. N. Basov, *Nano Lett.* **2021**, *21*, 5767.

[15] a) J. D. Caldwell, A. V. Kretinin, Y. Chen, V. Giannini, M. M. Fogler, Y. Francescato, C. T. Ellis, J. G. Tischler, C. R. Woods, A. J. Giles, M. Hong, K. Watanabe, T. Taniguchi, S. A. Maier, K. S. Novoselov, *Nat. Commun.* **2014**, *5*, 5221; b) Z. Jacob, *Nat. Mater.* **2014**, *13*, 1081; c) E. E. Narimanov, A. V. Kildishev, *Nat. Photonics* **2015**, *9*, 214; d) G. Hu, J. Shen, C. W. Qiu, A. Alù, S. Dai, *Adv. Opt. Mater.* **2020**, *8*, 1901393.

[16] a) A. K. Geim, I. V. Grigorieva, *Nature* **2013**, *499*, 419; b) S. Dai, Q. Ma, M. K. Liu, T. Andersen, Z. Fei, M. D. Goldflam, M. Wagner, K. Watanabe, T. Taniguchi, M. Thiemens, F. Keilmann, G. C. A. M. Janssen, S. E. Zhu, P. Jarillo-Herrero, M. M. Fogler, D. N. Basov, *Nat. Nanotechnol.* **2015**, *10*, 682; c) K. S. Novoselov,

A. Mishchenko, A. Carvalho, A. H. Castro Neto, *Science* **2016**, *353*, aac9439; d) S. J. Liang, B. Cheng, X. Cui, F. Miao, *Adv. Mater.* **2020**, *32*, 1903800.

[17] a) Q. Zhang, Q. Ou, G. Hu, J. Liu, Z. Dai, M. S. Fuhrer, Q. Bao, C.-W. Qiu, *Nano Lett.* **2021**, *21*, 3112; b) J. Duan, G. Álvarez-Pérez, A. I. F. Tresguerres-Mata, J. Taboada-Gutiérrez, K. V. Voronin, A. Bylinkin, B. Chang, S. Xiao, S. Liu, J. H. Edgar, J. I. Martín, V. S. Volkov, R. Hillenbrand, J. Martín-Sánchez, A. Y. Nikitin, P. Alonso-González, *Nat. Commun.* **2021**, *12*, 4325; c) J. Martín-Sánchez, J. Duan, J. Taboada-Gutiérrez, G. Álvarez-Pérez, K. V. Voronin, I. Prieto, W. Ma, Q. Bao, V. S. Volkov, R. Hillenbrand, A. Y. Nikitin, P. Alonso-González, *Sci. Adv.* **2021**, *7*, eabj0127; d) Z. Zheng, J. Jiang, N. Xu, X. Wang, W. Huang, Y. Ke, H. Chen, S. Deng, *Adv. Mater.* **2022**, *34*, 2104164.

[18] S. Dai, Q. Ma, Y. Yang, J. Rosenfeld, M. D. Goldflam, A. McLeod, Z. Sun, T. I. Andersen, Z. Fei, M. Liu, Y. Shao, K. Watanabe, T. Taniguchi, M. Thiemens, F. Keilmann, P. Jarillo-Herrero, M. M. Fogler, D. N. Basov, *Nano Lett.* **2017**, *17*, 5285.

[19] a) Z. Zheng, N. Xu, S. L. Oscurato, M. Tamagnone, F. Sun, Y. Jiang, Y. Ke, J. Chen, W. Huang, W. L. Wilson, A. Ambrosio, S. Deng, H. Chen, *Sci. Adv.* **2019**, *5*, eaav8690; b) S.-J. Yu, Y. Jiang, J. A. Roberts, M. A. Huber, H. Yao, X. Shi, H. A. Bechtel, S. N. G. Corder, T. F. Heinz, X. Zheng, J. A. Fan, *ACS Nano* **2022**, *16*, 3027.

[20] a) R. Fischer, K. Mason, *Proc. SPIE* **1987**, *0766*, https://doi.org/10.1117/12.940203; b) R. Fischer, K. Mason, *Proc. SPIE* **1989**, *1013*, https://doi.org/10.1117/12.949374.

[21] a) H. Hu, F. Zhai, D. Hu, Z. Li, B. Bai, X. Yang, Q. Dai, *Nanoscale* **2015**, *7*, 19493; b) B. Yao, Y. Liu, S.-W. Huang, C. Choi, Z. Xie, J. F. Flores, Y. Wu, M. Yu, D.-L. Kwong, Y. Huang, Y. Rao, X. Duan, C. W. Wong, *Nat. Photonics* **2018**, *12*, 22.

[22] a) H. Liu, Y. Liu, D. Zhu, *J. Mater. Chem.* **2011**, *21*, 3335; b) H. Hu, N. Chen, H. Teng, R. Yu, Y. Qu, J. Sun, M. Xue, D. Hu, B. Wu, C. Li, J. Chen, M. Liu, Z. Sun, Y. Liu, P. Li, S. Fan, F. J. García de Abajo, Q. Dai, arXiv:2201.00930, **2022**.

[23] a) E. H. Hwang, S. Adam, S. D. Sarma, *Phys. Rev. B* **2007**, *76*, 195421; b) F. Schedin, A. K. Geim, S. V. Morozov, E. W. Hill, P. Blake, M. I. Katsnelson, K. S. Novoselov, *Nat. Mater.* **2007**, *6*, 652; c) H. Hu, X. Yang, X. Guo, K. Khaliji, S. R. Biswas, F. J. García de Abajo, T. Low, Z. Sun, Q. Dai, *Nat. Commun.* **2019**, *10*, 1131; d) H. Hu, R. Yu, H. C. Teng, D. B. Hu, N. Chen, Y. P. Qu, X. X. Yang, X. Z. Chen, A. S. McLeod, P. Alonso-González, X. D. Guo, C. Li, Z. H. Yao, Z. J. Li, J. N. Chen, Z. P. Sun, M. K. Liu, F. J. García de Abajo, Q. Dai, *Nat. Commun.* **2022**, *13*, 1465.

[24] J. Kischkat, S. Peters, B. Gruska, M. Semtsiv, M. Chashnikova, M. Klinkmüller, O. Fedosenko, S. Machulik, A. Aleksandrova, G. Monastyrskyi, Y. Flores, W. T. Masselink, *Appl. Opt.: Opt. Technol. Biomed. Opt.* **2012**, *51*, 6789.

[25] S. Babar, J. H. Weaver, *Appl. Opt.* **2015**, *54*, 477.

[26] B. Wunsch, T. Stauber, F. Sols, F. Guinea, *New J. Phys.* **2006**, *8*, 318.

[27] M. Chen, X. Lin, T. H. Dinh, Z. Zheng, J. Shen, Q. Ma, H. Chen, P. Jarillo-Herrero, S. Dai, *Nat. Mater.* **2020**, *19*, 1307.

[28] H. Hu, X. Yang, F. Zhai, D. Hu, R. Liu, K. Liu, Z. Sun, Q. Dai, *Nat. Commun.* **2016**, *7*, 12334.